Ab-initio based models for temperature-dependent magneto-chemical interplay in bcc Fe-Mn alloys

Anton Schneider, Chu Chun Fu, Osamu Waseda, Cyrille Barreteau, Tilmann Hickel

Ab initio based models for temperature-dependent magnetochemical interplay in bcc Fe-Mn alloys

Anton Schneider,[1] Chu-Chun Fu,[1] Osamu Waseda,[2] Cyrille Barreteau,[3] and Tilmann Hickel[2]
[1]*Université Paris-Saclay, CEA, Service de Recherches de Métallurgie Physique, 91191 Gif-sur-Yvette, France*
[2]*Max-Planck-Institut für Eisenforschung, Düsseldorf 40237, Germany*
[3]*DRF-Service de Physique de l'Etat Condensé, CEA-CNRS, Université Paris-Saclay, F-91191 Gif-sur-Yvette, France*

(Received 24 July 2020; accepted 24 December 2020; published 14 January 2021)

Body-centered cubic (bcc) Fe-Mn systems are known to exhibit a complex and atypical magnetic behavior from both experiments and 0 K electronic-structure calculations, which is due to the half-filled 3*d* band of Mn. We propose effective interaction models for these alloys, which contain both atomic-spin and chemical variables. They were parameterized on a set of key density functional theory (DFT) data, with the inclusion of noncollinear magnetic configurations being indispensable. Two distinct approaches, namely a knowledge-driven and a machine-learning approach have been employed for the fitting. Employing these models in atomic Monte Carlo simulations enables the prediction of magnetic and thermodynamic properties of the Fe-Mn alloys, and their coupling, as functions of temperature. This includes the decrease of Curie temperature with increasing Mn concentration, the temperature evolution of the mixing enthalpy, and its correlation with the alloy magnetization. Also, going beyond the defect-free systems, we determined the binding free energy between a vacancy and a Mn atom, which is a key parameter controlling the atomic transport in Fe-Mn alloys.

DOI: 10.1103/PhysRevB.103.024421

I. INTRODUCTION

Thermodynamic and kinetic properties of Fe-based alloys can be strongly influenced by magnetism. For instance, previous studies have shown that magnetism in Fe-Cr alloys has a crucial impact on the mixing enthalpy and induces an asymmetry in the mutual solubility of Fe and Cr at low temperature [1,2]. It is also believed that, for a large range of concentrations in Fe-Co alloys, the ferromagnetic-paramagnetic (FM-PM) transition is closely linked to the body-centered-cubic (bcc) to face-centered-cubic (fcc) structural transition [3–5]. In fcc Fe-Mn alloys stacking-fault energies strongly depend on magnetic order [6]. Also, it is clearly known from experiments that the FM-to-PM transition in a bcc Fe system induces an abrupt acceleration of the diffusion of Fe and most of solute [7–17]. Among the binary Fe alloys, the Fe-Mn system exhibits some special behavior related to the half-filled 3*d* band of Mn. For example, the typical diffusion acceleration around the Curie point is not visible for Mn solutes in bcc Fe [7,18]. Pure bulk Mn itself shows a complex magnetostructural phase diagram [19,20]. Further, a strong magnetoelastic coupling in Fe-Mn alloys was raised previously [21]. However, so far, the magnetothermodynamic and magnetokinetic interplays in Fe-Mn systems remain unclear.

This study is focused on bcc Fe-Mn, since we are mainly interested in the Fe-rich part of this alloy. As can be seen in the equilibrium phase diagram from, for example, Witusiewicz *et al.* [22] and Bigdeli *et al.* [23], the stable domain of bcc Fe-Mn is limited to the dilute region (at most 5 at. % Mn). Despite the restricted homogeneity region, bcc Fe-Mn presents some intriguing properties, such as an extremely environment-dependent magnetic state of Mn solutes [24,25] and the anomalous Mn-solute diffusion behavior in bcc Fe-Mn. An accurate finite-temperature modeling of properties in this system that properly account for magnetic effects is highly necessary but challenging.

Up to now, mainly two distinct modeling approaches have been employed for the study of magnetic alloys at finite temperatures. On one hand, the disordered local moment (DLM) approach [26–31], often combined with the coherent potential approximation (CPA), allows one to describe alloys with both chemically and magnetically random structures, in order to mimic an ideal paramagnetic solid solution occurring at high temperatures. Recently, the itinerant coherent potential approximation (ICPA) has also been employed for the description of the PM state [32]. Some DLM studies were also carried out adopting supercells. For instance, a spin-space average approach was used to describe the disordered magnetic state [1,33,34]. Note that magnetic short range orders (SRO) are usually not taken into account in these approaches, and that the temperature evolution of the alloy properties cannot be directly predicted.

The other methodology, based on the parametrization of effective interaction models (EIMs) containing a magnetic and a chemical contributions has also shown interesting results for the study of materials properties as functions of temperature. Namely, Pierron-Bohnes *et al.* have used such an approach, based on the Ising model, in an early study on Fe-Co alloys [35]. A more sophisticated magnetic cluster expansion (MCE) approach was later applied by Lavrentiev *et al.* to the study of Fe-Ni [36], Fe-Cr [37], and Fe-Ni-Cr [38] alloys. Similar models were also developed by Ruban *et al.* [28] for Fe-Cr and by Tran *et al.* [39] for Fe-Co alloys. These models are generally used in on-lattice Monte Carlo (MC) simulations for finite temperature studies, Chapman *et al.* [40] have recently adapted the MCE model by Lavrentiev *et al.* [37] for spin-lattice dynamics simulations. The latter simulation technique

is exempted from the rigid-lattice constraint but is computationally much more demanding.

So far, such effective models have mostly been employed for the prediction of magnetic properties rather than thermodynamic properties such as phase diagrams. The simulations for the former are usually performed at fixed atomic structures, where only the magnetic structure evolves. This is mainly due to the complexity and high computational cost of MC simulations if dealing with a coupled evolution of both chemical and magnetic degrees of freedom. Moreover, the available models are limited to defect-free alloys, which prevents us from modeling kinetic properties.

In order to investigate the full interplay between magnetism and thermodynamic and defects properties for bcc Fe-Mn alloys, we aim at developing an effective interaction model, fitted on *ab initio* results, which takes all the relevant chemical and magnetic variables explicitly into account. Because the Mn magnetic moments exhibit significant magnitude variations for different local chemical environments, and in a highly complex way, the magnetic-interaction part of our model is based on a generalized Heisenberg formalism [1,37]. We first obtained a model for ideal Fe-Mn alloys. Then, as real materials are never defect-free, we also modified the obtained defect-free EIM to include the presence of a vacancy, as previously done for bcc Fe [17]. Being the simplest of the structural defects, vacancies play a crucial role in the atomic transport in Fe alloys. Note that magnetic properties of Fe and Mn atoms and the chemical interactions can significantly change around a vacancy [25].

An accurate parametrization procedure of such EIMs is generally a nontrivial task. In this paper, we propose two different strategies: The first one relies on the knowledge of key properties of the system, identified from prior density functional theory (DFT) results. The second one applies a machine-learning approach. Both resulting models [respectively, knowledge-driven (KD) and machine-learning (ML) models] are compared for quality assessment, and advantages and drawbacks of the two approaches are derived and discussed.

The paper is organized as follows: Section II describes details of DFT calculations for the models parametrizations and of Monte Carlo simulations for finite-temperature studies. The two strategies for the parametrization of EIMs are explained in Sec. III, and the accuracy of the obtained models are verified in Sec. IV. Then, the EIMs are applied (in Sec. V) to the prediction of various temperature-dependent properties that cannot be accessed directly from DFT calculations. As much as possible, the agreement with experimental or Calphad results is discussed.

II. COMPUTATIONAL METHODS

Throughout the paper, magnetic moments are expressed in Bohr magnetons and the model parameters are energies, expressed in meV.

A. Density functional theory calculations

In this work, density functional theory (DFT) calculations are performed in order to parametrize the effective interaction models. Although a full description of these calculations and the results is given in Ref. [25], we provide the key features in this section.

The DFT calculations are performed using the projector augmented wave (PAW) method [41,42] as implemented in the VASP (Vienna *ab initio* simulation package) code [43–45]. The results presented are obtained using the generalized gradient approximation (GGA) for the exchange-correlation functional in the Perdew-Burke-Ernzerhof (PBE) form [46]. All the calculations are spin polarized. $3d$ and $4s$ electrons are considered as valence electrons. The plane-wave basis cutoff is set to 400 eV. Atomic magnetic moments are obtained by a charge and spin projection onto the PAW spheres [44,45] as defined by the PAW potentials.

The k-point grids used in our calculations were adjusted according to the size of the supercell. They were chosen to achieve a k sampling equivalent to a bcc cubic unit cell with a $16 \times 16 \times 16$ shifted grid, following the Monkhorst-Pack scheme [47]. The Methfessel-Paxton broadening scheme with a 0.1 eV width was used [48]. The convergence threshold for the electronic self-consistency loop was set to $\Delta \mathrm{E} = 10^{-6}$ eV and atomic position relaxations with conservation of the total volume of the system were performed down to a maximum residual force of 0.02 eV/Å. We have verified that the magnetic structures and cluster formation energies are well converged with respect to the choice of k-point grids and the cutoff conditions. The resulting error bars for energy differences and magnetic moments of Fe and Mn are, respectively, 0.02 eV, 0.01 μ_{B}, and 0.1 μ_{B}. These are mainly associated to the convergence of the plane-wave energy cutoff and the k-grid density. All the alloy concentrations given in the paper are expressed as atomic percent, if not explicitly otherwise indicated.

Our fitting database consists in various systems containing Mn. Some are simply isolated Mn solutes Mn dimers at various distances (up to 8*nn*) in the Fe lattice, providing crucial information on the magnetic behavior of Mn solutes in a highly diluted environment and the behavior of the surrounding Fe magnetic moments. The dataset also contains random solid solutions over the whole range of concentrations (along with B2 and L12 ordered phases) whose mixing enthalpy is crucial to determine the phase separation and ordering tendency of the alloy. These tendencies are indeed the basis of alloys thermodynamic properties. Finally, the dataset also contains clusters from 3 to 15 Mn atoms with various magnetic states each. Since bcc Fe-Mn exhibit an unmixing tendency, the presence of these clustered configurations in the dataset is also very important to model the magnetic preferences of Mn atoms in these clusters during the decomposition. The random solid solutions are modeled using special quasirandom structures (SQS) which are obtained by generating 100 random configurations and selecting the lowest short range order among these. For each of these systems, several magnetic configurations have been generated. We note that, for isolated Mn solutes and Mn dimers in pure Fe, various noncollinear magnetic configurations were also considered. Considering the various chemical and magnetic configurations, the fitting database contains approximately 20 dimer configurations, 20 Fe-Mn

SQS systems, and one hundred Mn-cluster configurations. For more details, see Ref. [25].

B. Monte Carlo simulations

All the Monte Carlo (MC) simulations presented in this work are performed on a 16 000 atoms system assuming a bcc lattice ($20 \times 20 \times 20$ cubic unit cells). Random solutions are generated by randomly distributing p Mn atoms in the Fe matrix, where p is defined as the total number of atoms multiplied by the imposed Mn atomic concentration. In these simulations, the number of atoms is sufficiently large to ensure a proper random distribution of local environments. It has been checked that the results do not depend on the distribution of atoms in random solutions. For each simulation, 5×10^8 initial spin equilibration Metropolis attempts are performed in order to thermalize the magnetic structure. In the most difficult case, the convergence is reached after approximately 10^8 steps. For the spin-MC simulations at a fixed atomic configuration, we perform additional 4×10^8 MC steps for data collection.

In the simulations involving both magnetic equilibrations and atomic exchanges (namely spin-atom MC), after the spin thermalization, we perform a Metropolis attempt to exchange the respective positions of two randomly chosen atoms, once every N_s spin-MC steps. Convergence tests were done in order to ensure that enough spin-MC steps are performed between two successive atom-exchanges attempts. In the present calculations, 100 spin-MC attempts are carried out randomly anywhere in the system and 500 spin-MC attempts are performed in the two nearest-neighbor shells of the exchanged atoms.

In the presence of a vacancy, we follow a Monte Carlo method proposed in our previous study [17] which allows to determine the vacancy formation magnetic free energy as a function of temperature. The overall principle is that two separate subsystems are considered with the first one frozen at the FM state, while the magnetic configuration of the second one is allowed to evolve according to temperature. The vacancy is allowed to visit each site of the two subsystems via the Metropolis algorithm. Note that when the vacancy goes from one subsystem to the other, the resulting energy change should also account for the fact that the energy of an Fe atom (calculated by dividing the total energy of the system by the number of atoms composing it) at each temperature, is generally different in both subsystems. This total energy of the system results from an average of the total energy over 100 million spin-MC steps (different spin configurations) after thermalization of spins. Then, based on the relative number of visits to the two systems and the vacancy formation energy at the FM state, which is known to be 2.20 eV. Since in this study the vacancy properties are studied at the dilute Mn limit, we only consider the vacancy of Fe, which we believe to be a reasonable approximation, and the energy per atom calculated as it is described above is practically the same as the energy of an Fe atom. More details can be found in Ref. [17].

Please note that the lattice vibrational entropies are not intrinsically accounted for in the present EIM Monte Carlo setup. When necessary, they can be calculated additionally using DFT, in a similar way as in Ref. [17]. In the present study, we neglected spin-orbit coupling both in the DFT calculations and MC simulations because the effect is generally weak in these systems, when focusing on bulk properties [49–51].

III. EFFECTIVE INTERACTION MODEL

In this study, the EIMs adopt a Hamiltonian within the same formalism as in Refs. [36,37]. It is composed of a magnetic part, which includes an onsite term and a Heisenberg-like term and a pairwise chemical (nonmagnetic) interaction part.

The Hamiltonian has the following formal expression:

$$H = \sum_{i}^{N} \left(A_i M_i^2 + B_i M_i^4 + C_i M_i^6\right) + \sum_{i}^{N}\sum_{n}^{P}\sum_{j}^{Z_n} J_{ij}^{(n)} \mathbf{M}_i \cdot \mathbf{M}_j + \sum_{i}^{N}\sum_{n}^{P}\sum_{j}^{Z_n} V_{ij}^{(n)} \sigma_i \cdot \sigma_j, \tag{1}$$

where N is the total number of atoms, P is the maximum range of interactions in terms of neighbor shells, Z_n is the coordination number of each neighboring shell, $\mathbf{M}_i$ is the magnetic moment of the ith atom, M_i is its magnitude. $V_{ij}^{(n)}$ and $J_{ij}^{(n)}$ represent, respectively, the chemical pair interaction and the magnetic exchange-coupling parameters between atoms i and j, at a range n. As shown in the Appendix, these interaction parameters $V_{ij}^{(n)}$ and $J_{ij}^{(n)}$ depend on the chemical species of the ith and the jth atoms. σ_i is the occupation of the ith site, whose value is 1 if there is an atom on the site, and 0 if there is a vacancy. Note that since every pair interaction is counted twice, the $1/2$ factor is included in the pairwise interaction parameters ($V_{ij}^{(n)}$ and $J_{ij}^{(n)}$) listed in the Appendix.

A_i, B_i, and C_i are the magnetic onsite parameters of the ith atom. In order to keep this model as simple as possible, only three terms are considered in the magnetic onsite terms. Their role is to prevent the divergence of the magnetic moment magnitudes caused by the spin longitudinal variations due to the Heisenberg-like terms.

We use the DFT data described in Sec. II A to determine the free parameters. We present, in the following subsections, the two models fitted on the same DFT dataset and based essentially on the same Hamiltonian but resulting from the two different parametrization strategies.

A. Knowledge-driven (KD) model

For this model, we have chosen to determine the free parameters guided by key characteristics of this system that are revealed by the DFT investigations. In particular (i) in the presence of a magnetic frustration, the Mn-Mn interaction generally dominates over the Fe-Mn AF tendency, and (ii) the presence of two magnetic minima for a Mn solute, with their relative stability highly dependent on the local chemical environment [25].

A least-squares fitting method is applied. As the problem is over-determined, we applied a progressive parametrization procedure to reproduce a large number of physical properties derived from the DFT calculations. To this end, a priority is given to those data we consider to be the most important and

compromises are accepted for less relevant properties as, e.g., NM Fe.

The procedure consists of fitting first the magnetic-interaction parameters of pure Fe and pure Mn on the respective bulk magnetic properties. In a second step, we fit the Fe-Mn magnetic interactions parameters, keeping the pure-system parameters fixed. In order to fit these magnetic parameters, we use the DFT-predicted energy difference between systems with identical atomic configurations but distinct magnetic states. It allows us to attribute the total energy difference to the variation of the magnetic state. As the EIM will be applied to on-lattice MC simulations, any deviation from the perfect bcc structure due to atomic relaxations in the DFT calculations is not explicitly considered, but its effect on the total energy is taken into account in the energy differences. Finally, once a satisfactory set of magnetic parameters is found, the nonmagnetic parameters (associated to chemical bonding) are fitted on the DFT predicted mixing energies of Fe-Mn random solutions, represented by special quasirandom structures (SQSs).

1. Magnetic parameters from pure bcc Fe and bcc Mn properties

The Fe-Fe magnetic exchange-coupling parameters (J_{ij}s) and the onsite parameters (A_{Fe} and B_{Fe}, for the sake of simplicity $C_{\mathrm{Fe}} = 0$) are determined by using energies from DFT calculations performed on pure Fe systems (128-atom supercells) with various magnetic states. The J_{ij}s are fitted up to the fifth nearest-neighbor (5*nn*) shell. The systems used in our DFT study include ferromagnetic (FM), antiferromagnetic (AF), double-layer antiferromagnetic (AFD), quadruple-layer antiferromagnetic (AF4), nonmagnetic (NM), and also tens of magnetically disordered systems (random collinear magnetic moments). For the magnetically ordered structures, the calculations are performed using the corresponding equilibrium lattice constant (a_0). For the magnetically disordered structures, the FM equilibrium a_0 was assumed. We checked that the residual pressure remains lower than 10 kbar. We note that the obtained set of J_{ij}s is highly consistent with an earlier literature study [52].

Since we are mainly interested in the Fe-rich region of bcc Fe-Mn alloys, an accurate description of bcc Mn bulk properties is not a priority. However, it is still necessary to fit correctly the Mn magnetic parameters (A_{Mn}, B_{Mn}, and J_{ij}s, for the sake of simplicity $C_{\mathrm{Mn}} = 0$) in order to predict properly the interaction between various Mn solutes and the Mn clustering in the Fe lattice. We fit these interaction parameters on DFT data of pure bcc Mn in a similar way as for the Fe parameters. The J_{ij}s are also considered up to the fifth neighbor shell.

Please note that the relative values of Fe-Mn and Mn-Mn J_{ij}s control the competition of these interactions in the presence of a magnetic frustration. They have a critical effect in the determination of the magnetic ground state of Fe-Mn systems, especially when Mn clusters are present. Therefore, in practice, the obtained Mn-Mn parameters are slightly adjusted once the Fe-Mn J_{ij}s are determined.

Figure 1 shows the curves of the magnetic onsite energy imposed by the magnetic onsite terms as a function of the magnetic moment magnitude for Fe and Mn atoms. The onsite energies A_i, B_i, and C_i in Eq. (1) do not depend on the magnetic environment. As can be noticed in Fig. 1, the minimum of the Mn curve is more shallow and flatten than the one of Fe. This is consistent with DFT data [25] indicating that the magnetic moment magnitude of Mn atoms is much more dispersed than the ones of Fe atoms, for different local environments.

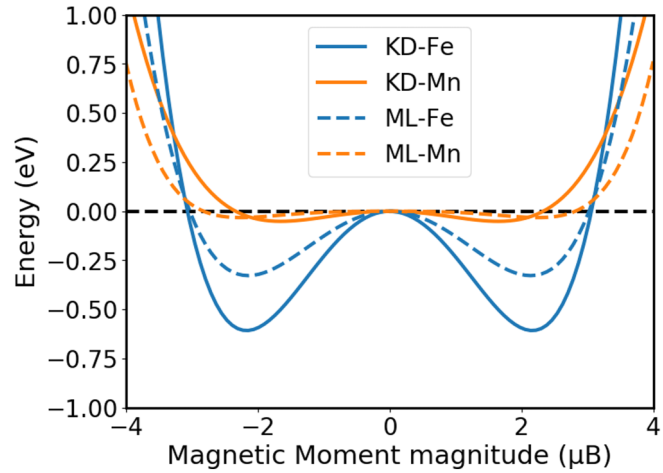

FIG. 1. Evolution of the magnetic onsite energy as a function of the magnetic moment magnitude. The magnitude of Fe spins is stiffer than the magnitude of Mn spins.

Figure 2 shows the model prediction of the energy difference between the respective magnetic ground state and various ordered magnetic states of pure bcc Fe and bcc Mn, using the final sets of parameters. For a close comparison, the DFT magnetic configurations are used as input for the EIM. The comparison with DFT results shows that the energy hierarchy of the various ordered magnetic states is well reproduced, while some deviations in quantitative energy values (in particular for NM-Fe) result from a compromise of considering various materials properties.

2. Fe-Mn magnetic parameters

As for Fe-Fe and Mn-Mn magnetic parameters, the J_{ij}s between Fe and Mn spins are also considered up to the 5*nn* shell. They are obtained by fitting to DFT energy differences between Fe-Mn systems (namely isolated Mn solutes, small Mn clusters, and Fe-Mn random solutions) with the same atomic configuration but different magnetic structures. Fitting these parameters with random solutions over the whole range of concentrations offers a large amount of different local environments which allows to naturally sample more accurately the particularly complex variations of average Mn magnetism with Mn concentration. Also, since the Mn-Mn magnetic interactions are dominant over Fe-Mn ones, the magnetic properties of clusters are expected to be dictated mainly by Mn-Mn interaction parameters.

It is worth mentioning that the presence of a magnetic frustration can be partially resolved by two alternative solutions: Either decreasing the spins magnitudes or developing a noncollinear magnetic arrangement. Both features were found in the case of Fe-Cr systems [53]. For the Fe-Mn alloys, the antiferromagnetic tendency of Fe-Mn and Mn-Mn interactions, although weaker than the Fe-Cr case, can also induce the emergence of a magnetic frustration at low or intermediate

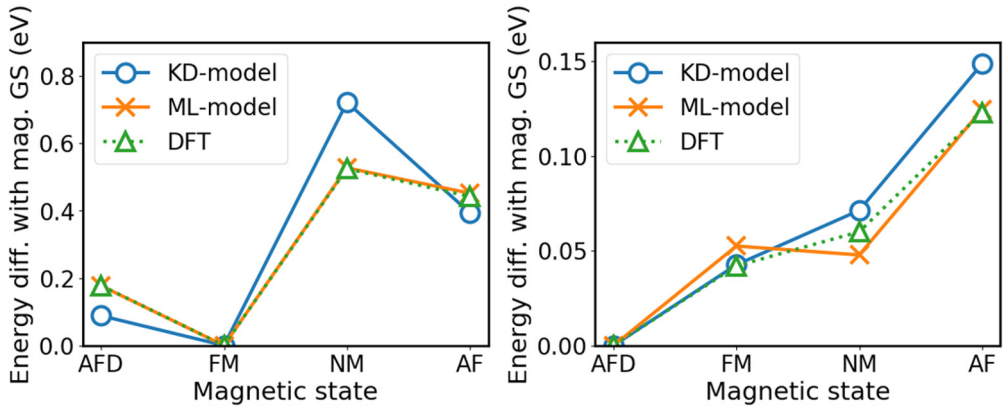

FIG. 2. Model predictions of the energy differences between ordered magnetic states of bcc Fe (left) and bcc Mn (right), using the magnetic moments predicted from DFT, compared to DFT results.

temperatures. We note that, using simple local-environment independent J_{ij}s, many noncollinear ground states are found when performing Monte Carlo simulations. These states are actually an artifact of the EIM, since their energies are significantly higher than those of other collinear states according to our DFT verification.

In order to solve this problem, we added to the Fe-Mn exchange-coupling parameters a spin-angle dependence, fitted to DFT noncollinear data obtained for an isolated Mn solute in bcc Fe [25] (Fig. 3). The principle is to add a penalty term $J_0^n \cdot \frac{\theta-90^\circ}{90^\circ}$ that depends on the angle θ between the Mn magnetic moment and the average magnetic moment of the Fe atoms in the two nearest-neighbor shells of the concerned Mn atom. Figure 3 presents the energy dependence of a systems with an isolated Mn atom in a FM Fe matrix on this angle θ. As can be observed, our expression allows to reproduce correctly the noncollinear barrier between the two collinear minima with the angle equal to 0°(FM-Mn) and 180°(AF-Mn).

In addition, as shown by DFT studies Ref. [25], it is specifically for Fe-Mn alloys very important to consider the dependence of the Fe-Mn magnetic-interaction trend on the Mn concentration in random solutions. In the dilute limit, the Fe-Mn interaction tends to be antiferromagnetic, while at higher concentration (above 7 at. % Mn) it becomes ferromagnetic. In order to properly reproduce this feature, a local concentration dependent term (fourth degree polynomial) is also added to the Fe-Mn J_{ij}s.

The final expression for the Fe-Mn exchange-coupling parameters is:

$$J^n_{\text{Fe-Mn}} = \left[J^n_0 \cdot \frac{\theta - 90^\circ}{90^\circ}\right] + a \cdot [\text{Mn}]^4_{\text{loc}} + b \cdot [\text{Mn}]^3_{\text{loc}} + c \cdot [\text{Mn}]^2_{\text{loc}} + d \cdot [\text{Mn}]_{\text{loc}} + e, \quad (2)$$

where the J^n_0 is the original $J^n_{\text{Fe-Mn}}$ parameter, before considering the angle and concentration dependencies. This parameter ensures the neighbor-shell dependence of the interaction (since the angle and concentration dependencies do not depend on the interatomic distance). $[\text{Mn}]_{\text{loc}}$ is the local Mn concentration in the five nearest-neighbor shells around the concerned atom.

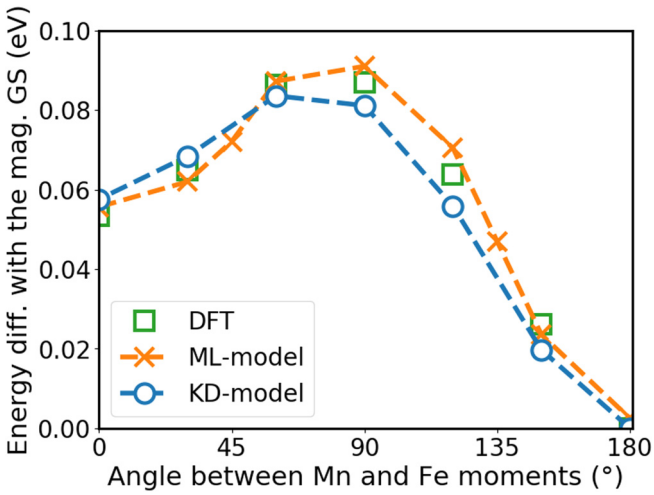

FIG. 3. Energy of an isolated Mn atom in a ferromagnetic Fe matrix with various angles compared to the Fe atoms. The ground-state configuration (Mn antiparallel to Fe) is chosen as a reference.

3. Nonmagnetic parameters

At this point, all the free parameters of the magnetic part of the Hamiltonian are determined and may be used to estimate the magnetic contribution of the energy difference between two systems. It is for instance possible to calculate the magnetic contribution to the mixing energy of Fe-Mn solid solutions at any concentration, using the following expression:

$$E^{\text{mix}}(\text{Fe-Mn}) = \frac{E^{\text{tot}}(n\text{Fe} + p\text{Mn}) - nE(\text{Fe}) - pE(\text{Mn})}{n+p}, \quad (3)$$

where $E^{\text{tot}}(n\text{Fe} + p\text{Mn})$ is the total energy of the Fe-Mn solid solution, $E(\text{Fe})$ is the energy per atom of pure bcc Fe (in its lowest energy magnetic state: FM), and $E(\text{Mn})$ is the energy per atom of pure bcc Mn.

The fitting of these nonmagnetic parameters is performed using the DFT Fe-Mn SQS systems, as they include a large number of different local environments. Also, mixing energies of these random alloys are a good indicator of the phase separation or ordering tendency of the alloy, which is one of the fundamental thermodynamic properties of alloys.

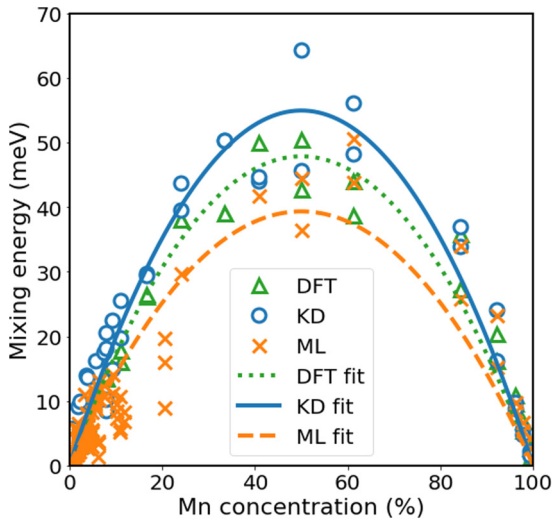

FIG. 4. Total mixing energy obtained from DFT calculations and the effective interaction model. The DFT configurations and magnetic moments have been used as input for the EIM.

The difference between the mixing energy obtained from DFT calculations (which includes magnetic and nonmagnetic contributions) and the magnetic contribution of the mixing energy from the EIM provides the nonmagnetic contribution of the mixing energy. Chemical parameters of the model are fitted to the latter in order to accurately reproduce the DFT total mixing energy with the model. Figure 4 shows the mixing energies obtained from DFT and also the mixing energies calculated with the KD and ML models, using the DFT magnetic and atomic configurations (without further relaxation).

B. KD model including a vacancy

With minor modifications, the obtained KD model can be extended to account for the presence of a small concentration of vacancies, represented by a Fe-Mn supercell containing a vacancy. We have verified that the adopted MC simulation cell (with 16 000 atomic sites) allows us to consider the vacancy as isolated and ensures the convergence of the various studied properties. In this work, we parametrize the model for Fe-Mn alloys that are very dilute in Mn. To do so, we follow a similar approach as described in Ref. [17] for the extremely dilute Fe-Cu-vacancy system. We note however that in the present case the effects of vacancies on the local magnetic moment of Mn solutes is more complex than what is observed with Cu solutes. As explained in Ref. [25], the presence of a vacancy highly favors the AF-Mn state to the detriment of FM-Mn. Such complexities have to be taken into account when parametrizing the interactions in the presence of a vacancy. Also, in Ref. [17] the model was parameterized for the extremely dilute case of one Cu solute and one vacancy in bcc Fe, while in the present case, the model was first parameterized without vacancies for various concentrations (see Sec. III A). Only then the parameters were adjusted to take into account the presence of a vacancy nearby a Mn solute, which makes the approach slightly different.

The overall principle is to preserve the parametrization obtained for the defect-free Fe-Mn system and to include some variations in the parameters for atoms near the vacancy. The onsite A_i and B_i parameters of both Fe and Mn species are modified for atoms located at the first and second nearest-neighbor (1*nn* and 2*nn*) shells of the vacancy in order to model the magnitude variation of the magnetic moments induced by the presence of a vacancy. Indeed, DFT results show that nearby a vacancy, the 1*nn* (resp. 2*nn*) Fe atoms magnetic moment magnitude tend to increase (resp. decrease) by 0.2 μ_B [17]. Also, J_0 parameters are modified for the atoms at 1*nn* and 2*nn* sites of the vacancy in order to capture the change of the relative energetic stability of the two magnetic minima of a Mn atom in Fe. For example, as predicted by DFT calculations [25], for an isolated Mn in Fe, the state with the Mn spin antiparallel to the Fe spins (AF-Mn) is 0.05 eV lower in energy than the state with the Mn spin parallel to the Fe spins (FM-Mn). But, if the Mn solute is at 1*nn* of a vacancy, this energy difference increases to 0.25 eV.

C. Machine-learning (ML) model

For the parametrization of the machine-learning model, a ridge regression approach was employed. Such a regression allows us to optimize the set of parameter β_i (representing $J_{ij}^{(n)}, V_{ij}^{(n)}$, etc.) belonging to the different terms h_j of the Hamiltonian (1) without evaluating the DFT data points individually. Within this technique an overfitting is avoided by adding penalty terms with Lagrange multipliers λ_j:

$$L(\boldsymbol{\beta}) = \sum_i \left(E_i - \sum_j \beta_j h_j(\mathbf{x}_i) \right)^2 + \sum_j \lambda_j \beta_j^2. \quad (4)$$

For the sake of consistency with the knowledge-driven model, the prediction only accounts for the same training set $\{\mathbf{x}_i, E_i\}_i$ of spin and chemical configurations together with their corresponding DFT energies, ignoring their derivatives and forces. As one of the consequences, the model does not necessarily reproduce the correct spin structure for the ground state in the Mn-rich regime.

Such kind of method has already been used to successfully predict interatomic interactions in nonmagnetic elemental metals after a training with thousands of DFT data [54–56]. Recently, a similar type of ML approach was employed to obtain a Heisenberg spin Hamiltonian [57]. Our regularization in the last term of Eq. (4) differs, however, from standard ML applications by the fact that various Lagrange multipliers λ_j are used to account for the different sizes and nature of the physical parameters β_j.

The regression is performed for the complete training set of collinear DFT data, but the selection of a proper starting point is subject to the two-step approach. Accordingly, the model parameters for pure Fe were fitted firstly to the DFT data containing only Fe atoms in collinear calculations. The parameters $\beta_j^{(0)}$ obtained in this step are then used as input parameters for the fitting of model parameters $\beta_j^{(0)} + \beta_j$ of the full model in the second step:

$$L(\boldsymbol{\beta}) = \sum_i \left(E_i - \sum_j \left(\beta_j^{(0)} + \beta_j\right) h_j(\mathbf{x}_i) \right)^2 + \sum_j \lambda_j \beta_j^2. \quad (5)$$

This two-step approach exploits the multivariate normal distribution of the prior probability distribution of the fit parameters following the Bayesian interpretation of the ridge regression [58]. In other words, the probability of finding the fit parameters for pure Fe in the second fitting step is given by normal distributions, for which the variance is given by the regularization factor. Finally, the noncollinear terms were determined separately via a standard least square method. For the ridge regression method, the data points were separated into 10 training sets, out of which one set was used for validation at each cross-validation step. The machine-learning model uses the same model Hamiltonian (1) as before with minor modifications as explained below.

1. Magnetic parameters for pure bcc Fe and Mn

In order to meet the above-mentioned challenges to reproduce the magnetic ground state in the Mn-rich regime, the onsite terms for the Mn magnetic moment magnitude involve A_{Mn}, B_{Mn}, and C_{Mn} terms [see Eq. (1)] whereas in the case of Fe the description is limited to the two onsite terms A_{Fe} and B_{Fe}. Fig. 1 shows the variation of energy per atom for the onsite terms as a function of the magnetic moment. As compared to the KD model, the stabilization of the Fe moment is slightly more pronounced, yielding almost the same moment magnitude. For the Mn atoms, however, the magnetic moments are even more dispersed than in the KD model, with hardly any change in the energy until the magnitude becomes relatively large ($|M| > 3$).

The two-step approach ensures that even after the regression with all collinear DFT results the ground states of pure Fe can be reproduced with an error per atom around 1 meV (cf. Fig. 2). We can see that the energy values for pure Mn were not reproduced with the same precision. This is also because the dataset mostly consists of Fe-rich DFT results, so that for the sake of reproducing Mn interactions embedded in Fe, the pure Mn interactions had to be compromised. As a consequence, the machine-learning model puts more emphasis on pure Fe than the KD approach, which yields the better description of pure FM Fe.

2. Fe-Mn pair-interaction parameters

The Fe-Mn Heisenberg parameters in the machine-learning model contain five different values for the first five shells, i.e., have the same form as for pure Fe and pure Mn. However, a correction term $c_{\mathrm{Mn}}\Delta J_{\mathrm{Fe\text{-}Mn}}$, which depends on the global Mn fraction in the system c_{Mn}, was added to each of the five Heisenberg parameters. This replaces all the terms in Eq. (2) that explicitly contain the local Mn concentration. Furthermore, an angle-dependent contribution $J_0^n|\mathbf{M}_{\mathrm{Mn}} \times \langle \mathbf{M}_{\mathrm{Fe}} \rangle|^2/|\mathbf{M}_{\mathrm{Mn}}|^2$, where $\langle \mathbf{M}_{\mathrm{Fe}} \rangle$ is the average magnetic moment of Fe, was added to each Mn atom.

Figure 3 shows the variation of the angle-dependent part for the Fe-Mn interactions. Similarly to the knowledge-driven model, it reproduces the noncollinear barrier from AF to FM spin structures as manifested by the DFT results.

For consistency with the KD-model, nonmagnetic interactions are considered up to the fifth nearest neighbor in the case of Mn-Mn interactions and up to the second nearest-neighbor for Fe-Mn and Fe-Fe interactions. Contrary to the fitting procedure of the KD model, these parameters are fitted altogether with the magnetic ones, by taking into account the differences of total energy between the various configurations obtained via DFT calculations. Together, the ML model contains fewer analytical terms for the composition dependence of the exchange-coupling parameters, consistent with the philosophy of an automatized machine-learning approach.

We note that values of the model parameters obtained with the two different fitting techniques largely differ in some cases by several orders of magnitude (e.g., $V_{\mathrm{Fe\text{-}Fe}}$) or even the sign (e.g., $J^{(3nn)}_{\mathrm{Fe\text{-}Fe}}$). In the case of the chemical interaction parameters, however, it is a consequence of different reference choices.

IV. GROUND-STATE PROPERTIES: ACCURACY OF THE MODELS

In this section, the accuracy of the two models is verified and discussed through a comparison with DFT results on properties of bcc Fe, bcc Mn, and bcc Fe-Mn systems. In each case, equivalent atomic configurations as in the DFT data are used, whereas the magnetic structures for the models are determined using Monte Carlo spin relaxations.

First, the distribution of Mn and Fe magnetic moments magnitudes, defined as: In random solutions up to 50 at. % Mn from DFT calculations [25] is shown in the top panel of Fig. 5. The magnetic moment magnitude M_i of an atom i is defined as:

$$M_i = \|\mathbf{M}_i\|, \tag{6}$$

where $\mathbf{M}_i$ is the magnetic moment of the atom i. The data reveal the complexity of Mn magnetism in bcc Fe, with very scattered magnetic moment magnitudes. The bottom panel of Fig. 5 shows the corresponding distribution obtained using the KD model along with spin Monte Carlo simulations at 10 K. Concerning the distribution of Fe magnetic moment magnitudes, the agreement between the two approaches is excellent. In the case of Mn, although it is difficult to model such a complex behavior with a simple model, both approaches show the same general trend: a maximum around 2.0 μ_B and a wider distribution than Fe.

Concerning the pure bcc Mn, when using the DFT predicted magnetic state as an input, the AFD state is properly predicted (with both KD and ML models) as the lowest energy magnetic state, compared to FM, AF, and NM states (see Fig. 2). However, when performing spin-MC simulations, both models cannot capture the direction-dependent magnetic interaction. Using the KD model, the magnetic ground state predicted by Monte Carlo simulation is a spin glass without any magnetic long-range order, whose energy is 0.02 eV/atom lower than the AFD ground state. Due to the limited number of DFT training data, this applies even stronger to the machine-learning model, which also shows a disordered magnetic state, which energy is 0.8 eV/atom lower than the AFD ground state.

Both EIMs allows us to properly simulate the concentration dependency of the Fe-Mn magnetic interaction tendency, as shown in Fig. 6, in comparison with DFT results. The change of average Mn magnetic state is also explicited by

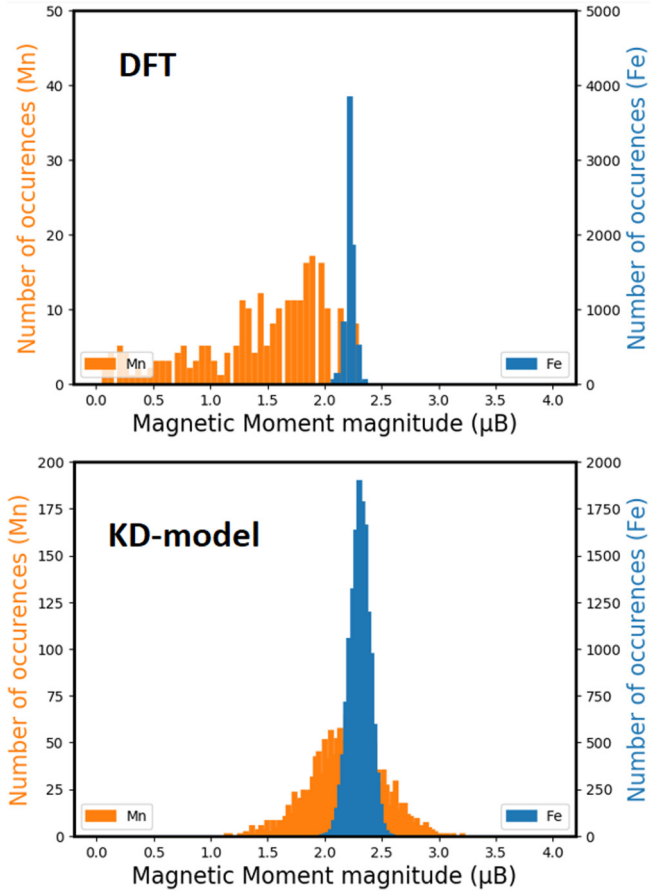

FIG. 5. Distribution of Fe and Mn local magnetic moments in Fe-Mn random alloys, up to 50 at. % Mn, using (top) DFT SQS calculations and (bottom) interaction model coupled with Monte Carlo simulations at 10 K.

the angle distribution of Mn magnetic moments compared to the average magnetic moment of Fe atoms. The results shown in Fig. 7 are obtained with spin Monte Carlo simulation

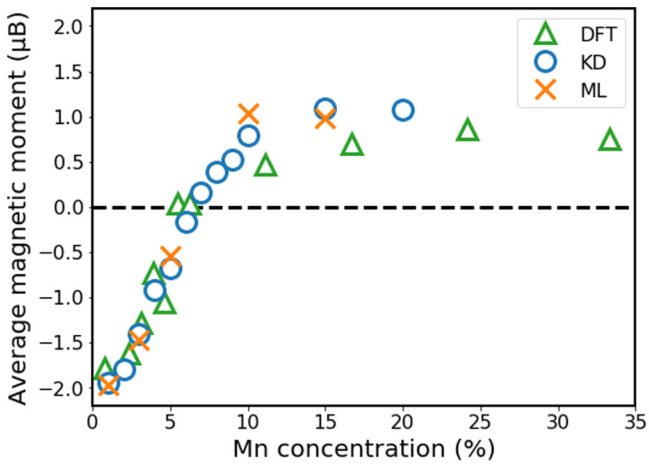

FIG. 6. Average magnetic moment of Mn atoms as a function of Mn concentration, from DFT calculations and spin Monte Carlo simulations at 10 K.

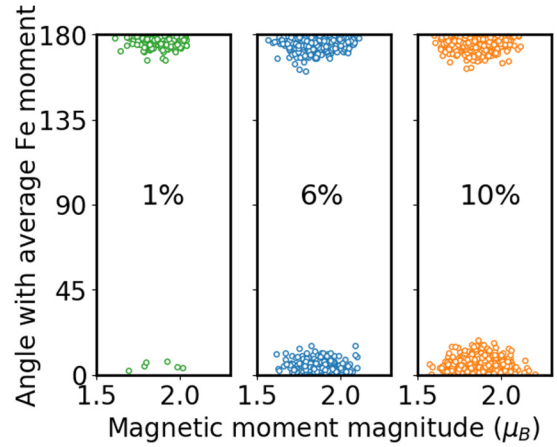

FIG. 7. Angle distribution between Mn magnetic moments and the average magnetic moment of Fe atoms, in random solutions at 1, 6, and 10 at. % Mn concentrations, using the KD model along with spin Monte Carlo simulations at 10 K.

at 10 K in random Fe-Mn solutions at 1, 6, and 10 at. % Mn, using the KD model. It is clear that at 1% the coupling tendency between Mn and Fe moments is antiferromagnetic while increasing the concentration favors more and more the ferromagnetic coupling. Also, in agreement with DFT predictions, noncollinear states are not predicted for such a low temperature.

As explained in Sec. III, the mixing energy of the Fe-Mn random solutions was used to parametrize the interaction parameters of the models. At that stage, the models were shown to correctly predict the mixing energies when adopting the magnetic moments of the DFT data (Fig. 4). Here, we investigate whether the EIMs can satisfactory predict mixing energies at their own magnetic ground states.

The concentration dependence of bcc Fe-Mn mixing energy is determined by generating Fe-Mn random alloys at various concentrations. The magnetic state of these random configurations is relaxed via spin Monte Carlo simulation at 1 K, while the atomic structure is kept constant in order to prevent the possible appearance of atomic short range order or any phase separation.

Within the KD model the bcc Mn reference state presents a spin glass as the lowest energy magnetic state, with an energy close to that of the DFT magnetic ground state. In case of the ML model, however, pure Mn and the Mn-rich region are less accurately captured (see Sec. III C). Therefore, in the latter case, we provide in Fig. 8 the mixing energy curves considering both the DFT and the ML-model magnetic ground states.

As can be seen in Fig. 8, the obtained mixing energies are positive for all concentrations with the KD model and are very close to the DFT data. When considering the ML model with the MC relaxed magnetic state for the pure Mn reference, all the mixing energies are positive although they exhibit too large values (about ten times larger than the KD model and the DFT data). The large difference between these two curves suggests how the fitting is penalized when the dataset shrinks. Indeed, we have performed most of our DFT calculations in the Fe-rich domain and only a few in the Mn-rich domain. Although the KD model is flexible enough to accommodate

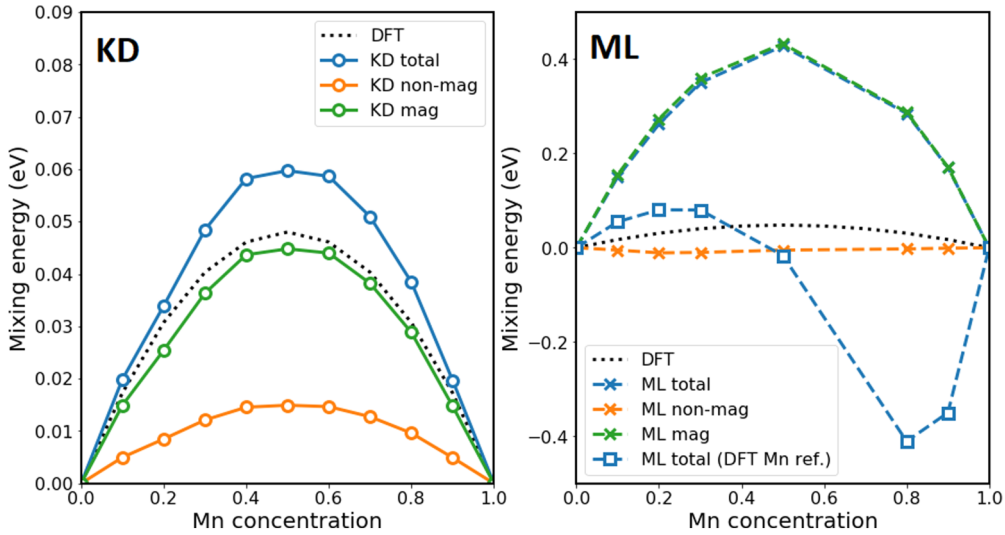

FIG. 8. Mixing energy of random solutions as a function of Mn atomic concentration. The black dotted line shows the results obtained with DFT for comparison, the blue line shows the total mixing energy obtained from $T = 1$ K spin-MC simulations, the green and the orange lines, respectively, show the magnetic and the nonmagnetic contributions of the mixing energy obtained via MC simulations.

to such a locally reduced dataset, the ML model exhibits spurious ground states in the Mn-rich domain which jeopardize the prediction of some properties (such as the mixing energy). To illustrate that, we also provide the mixing energy curve predicted by the ML model, using the DFT magnetic configuration for pure Mn. As a result, mixing energies of the Fe-rich part are in better agreement with DFT and KD model results (since the pure Mn reference is now properly described), but not the Mn-rich part which remains not accurately predicted. The dramatic difference induced by the change of pure-Mn reference energy suggests that the model would benefit from a more complete dataset in the Mn-rich domain. Accordingly the agreement with the present and previous [59] DFT results differs for both models. In particular, the results for the KD model indicate an unmixing tendency that is consistent with experimental evidences [60].

A qualitative difference between the two models can be observed when separating the magnetic and nonmagnetic contributions of the mixing energy, as shown in Fig. 8. Using the KD model, both magnetic and nonmagnetic contributions exhibit positive values with a similar order of magnitude (although the magnetic contribution shows larger values). Using the ML model, where both contributions are fitted simultaneously, the magnetic contributions are extremely dominant, whereas the nonmagnetic terms are negative with very small values.

This discrepancy between the two models illustrates that the number of DFT training data and the available information about the stability of input structures are insufficient to accurately describe mixing in an automized ML approach. To support the fact that artificial intelligence based approaches generally require extended datasets, the example of previous studies in Refs. [61,62] can be mentioned. These two studies lead to very similar conclusions concerning the precipitation kinetics in Fe-Cu bcc alloys, although the knowledge-driven one [61] considers a few tens of barriers while the machine-learning based study [62] requires 2000 barriers. At the same time, our results also indicate that the energetic properties are much more sensitive to the parametrization than the magnetic properties. The prediction of the latter is visibly more robust.

Besides the magnetic properties of the Fe-Mn random solutions, we have also verified the prediction of magnetic ground state of Mn clusters in bcc Fe, in view of the unmixing tendency of the alloy. We find that the two models correctly predict the DFT ground state of every Mn-cluster configuration from two to eight atoms (see Fig. 10 of Ref. [25]), except in the case of the 5-Mn cluster (see Fig. 9) where the ground state obtained from the EIM-MC simulation (using both the KD and the ML models) is found to be 0.01 eV/Mn less energetic than the ground state predicted by DFT calculations.

V. MODEL PREDICTIONS OF TEMPERATURE-DEPENDENT PROPERTIES

In this section, we provide examples to illustrate the applicability and accuracy of the present models, for the prediction of finite-temperature properties. We present the results of the KD model for all the properties. When relevant, the outcomes from the two models are compared. Such comparisons allow us to assess the robustness and quality of the predictions in scenarios for which DFT calculations are not feasible. The first four subsections address magnetic and thermodynamic

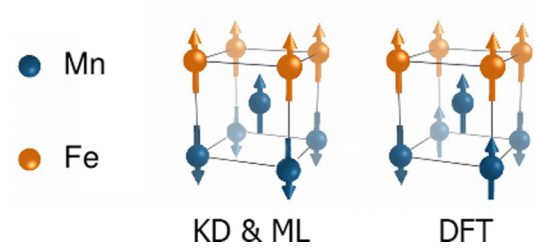

FIG. 9. Visualization of the magnetic ground state of the 5-Mn cluster as predicted using the models (both KD and ML) and DFT.

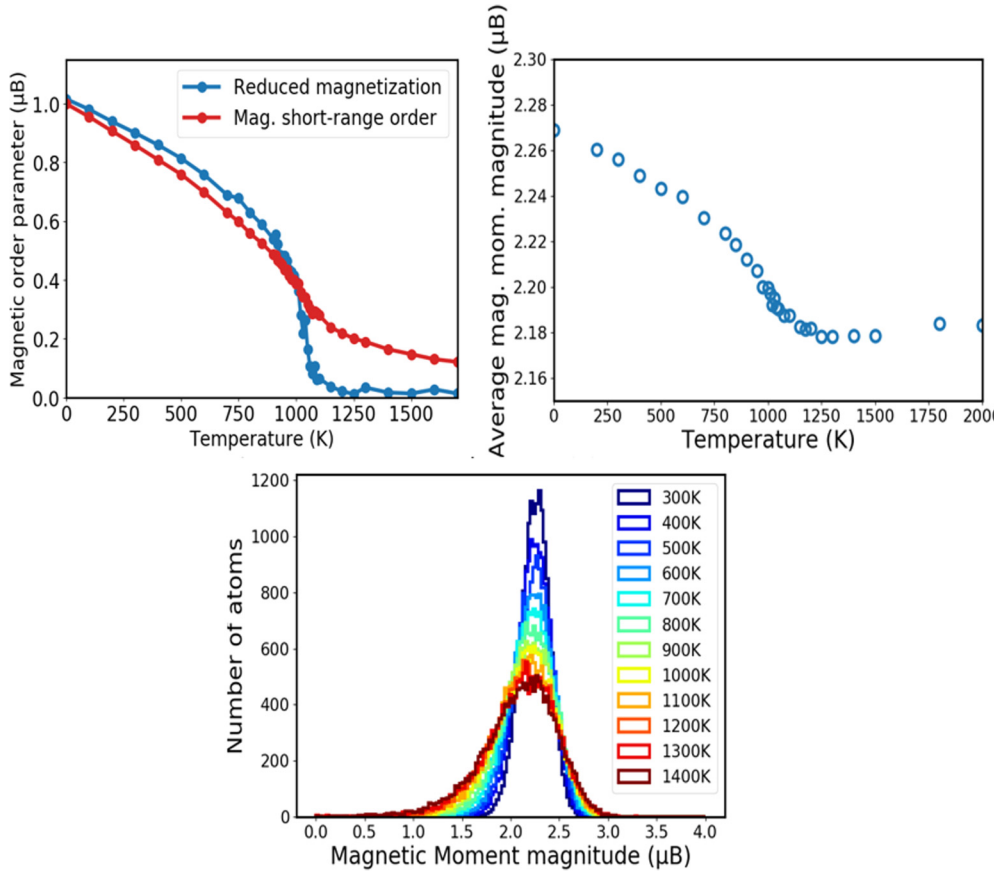

FIG. 10. (top left) Temperature evolution of the reduced magnetization and the 1*nn* magnetic short-range order in pure bcc Fe. (top right) Temperature evolution of the average magnetic moment magnitude of Fe atoms. (bottom) Distribution of the magnetic moment magnitude of Fe atoms for various temperatures. The three panels are produced using the KD model along with spin Monte Carlo simulations.

properties at fixed atomic configurations, via spin Monte Carlo equilibrations, while the last two subsections investigate the interplay between magnetic and chemical configurations, employing a coupled spin-atom MC simulations.

A. Temperature dependence of bcc Fe magnetic properties

First of all, the reduced magnetization M_R of pure Fe is shown in Fig. 10. At each temperature, it is calculated as

$$M_R = \left\| \frac{\langle \mathbf{M}_i \rangle}{\langle M_i \rangle} \right\|, \tag{7}$$

where $\langle \mathbf{M}_i \rangle$ is the average of the magnetic moment of all the atoms and $\langle M_i \rangle$ is the average of the magnetic moment magnitude of all the atoms. The calculated T_C is approximately 1060 K, compared to 1044 K obtained experimentally [63]. The result is almost the same for both models, indicating that the slight deviations for AFD and NM energies in the KD model (Fig. 2) have no impact on this property.

The 1*nn* magnetic short-range order (MSRO), defined here as the nearest-neighbor spin pair-correlation function, is also shown in Fig. 10. As can be noticed, in the low temperature domain (below T_C) it decreases with temperature slightly faster than the magnetization. On the opposite, at high temperature (beyond T_C), MSRO remains significant. These results are in good agreement with previous studies [64–66]. The significance of MSRO in both models, with only slightly larger values in the machine-learning model, indicates the robustness and physical relevance of this prediction. Therefore, the study of properties around T_C needs to take MSRO into account.

As shown in the upper panel of Fig. 10, the average magnitude of Fe magnetic moments decreases with temperature up to the Curie temperature. When $T > T_C$, the average magnitude increases very slightly with temperature. This curve is in good agreement with the results of Lavrentiev *et al.* [37] obtained with a similar approach. However, one should note that these variations of the average magnitude are very small (contained within 0.1 μ_B) which suggests that the classical Heisenberg model is a good approximation for pure Fe.

The resulting temperature evolution of the magnitude distribution, shown in the bottom panel of Fig. 10, is a direct consequence of the magnetic onsite terms shown in Fig. 1. The results are in good agreement with a study of Ruban *et al.* [1], performed with a similar approach.

B. Curie temperature of bcc Fe-Mn random solutions

The Curie temperature is a fundamental property of ferromagnetic systems. As our goal is to develop an effective interaction model, capable to describe properly the magnetothermodynamic properties of the bcc Fe-Mn alloys at any

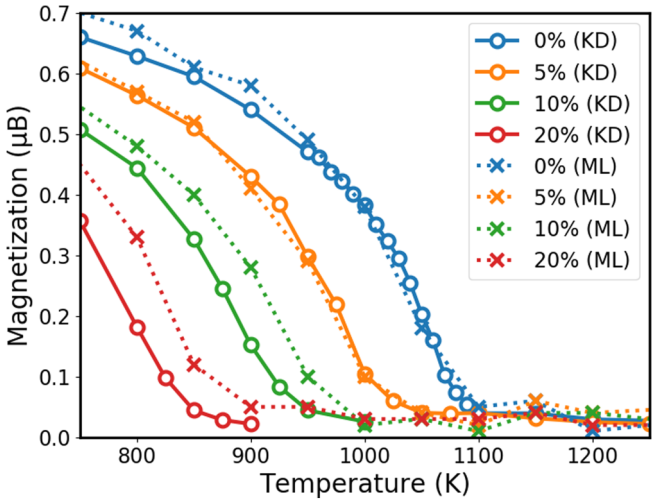

FIG. 11. Temperature evolution of the total magnetization, for various Mn atomic concentrations in the Fe-rich regime. The results of the KD model (solid lines) and the ML model (dashed lines) are compared.

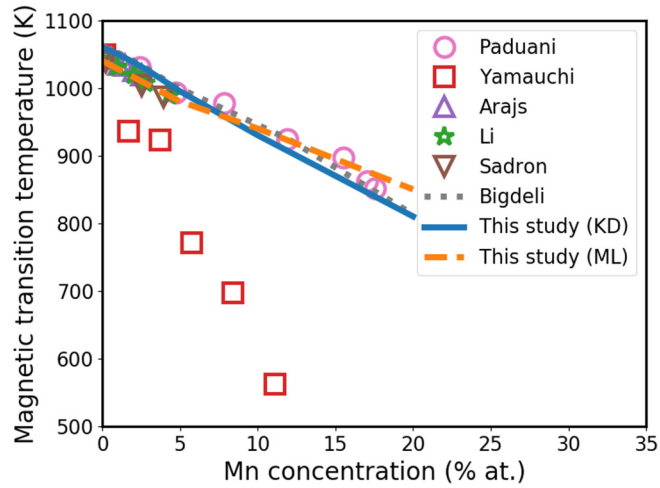

FIG. 12. Curie temperature of dilute bcc Fe-Mn alloys as a function of Mn concentration. The solid and dashed blue lines show our results while the symbols show literature experimental results. Circles: Paduani *et al.* [68], squares: Yamauchi *et al.* [72], upward triangles: Arajs *et al.* [69], stars: Li *et al.* [70], downward triangles: Sadron *et al.* [71]. Our results are also compared to a CALPHAD study shown with a dotted line: Bigdeli *et al.* [23].

given temperature, the Mn concentration dependence of T_C in the dilute Fe-Mn alloys is of great relevance.

In Fig. 11 the temperature dependence of total magnetization for various Mn concentrations in the Fe-rich regime is provided. The total magnetization M is defined as:

$$M = \|\langle \mathbf{M}_i \rangle\|, \tag{8}$$

where $\langle \mathbf{M}_i \rangle$ is the average of the magnetic moment of all the atoms. These calculations are all performed in random solutions. The magnetization curves are systematically shifted towards low temperatures with increasing Mn concentrations. For dilute bcc Fe-Mn alloys a remarkable agreement between both models is observed, despite the fact that even small differences in the analytical expressions of the Fe-Mn exchange-coupling parameters are used. For 10 and 20 at. % of Mn the shift is slightly stronger in the KD model as compared to the ML model.

We estimate the Curie temperature T_C as the inflection point of the $M(T)$ curve [67]. The T_C of each considered concentration is reported in Fig. 12 in order to compare with existing experimental results. As can be seen, T_C decreases with Mn concentration with a slope of approximately 10 K per Mn at. %, in excellent agreement with most literature data. Indeed, most experimental works have shown that T_C tends to decrease in the dilute limit linearly with Mn concentration, at a rate of approximately 10 K per Mn at. % [68–71], as shown in Fig. 12.

For intermediate compositions up to 20 at. % of Mn, deviating experimental trends are reported in the literature. While the slope of 10 K per Mn at. % continuous in the case of Paduani *et al.* [68], Yamauchi *et al.* [72] found a larger decreasing slope of around 43 K per Mn at. %.

One possible explanation for the deviation of Yamauchi *et al.* is that their magnetic measurements are biased by the use of cold rolling on the samples in order to stabilize the body-centered cubic phase [72], which is not the case in the other experimental studies. A recent study indeed suggests that a plastic deformation has a significant impact on the atomic short-range order of α-Fe-Mn systems [73], which according to our results may affect the magnetic configuration. We note that in order to stabilize α-Fe-Mn beyond 5 at. % Mn, Paduani *et al.* have added 3 at. % Ti to the solution [68]. As the low concentration results (below 5 at. % Mn) of Paduani *et al.* are in excellent agreement with the studies using pure Fe-Mn, it can be assumed that there is not significant effect of such Ti addition on the magnetic state of the solution. A recent Calphad assessment [23] also assumes such a decrease of T_C with Mn concentration at a rate of approximately 10 K per Mn at. %, as shown in Fig. 12.

As explained in the previous section, the analysis of the KD and ML models results shows that the magnetic ground state predicted by Monte Carlo simulation is a spin glass without any magnetic long-range order. Because of this, a Néel transition, which might occur in bcc Mn and in the Mn-rich limit of the alloy, is not reproduced. There is no experimental evidence of such a Néel transition because the bcc phase of pure Mn is only stable at very high temperature (between 1411 and 1519 K). However, as we have shown in a previous study that the DFT ground state of pure bcc Mn is AFD [25], we expect a magnetic transition, going from this state to the PM state. As we are mostly interested in the Fe-rich part, we believe it is not crucial here to properly describe such properties in the extremely Mn-rich domain.

C. Temperature dependence of Mn magnetic moment

As shown in Fig. 6, the average magnetic moment of Mn atoms in bcc Fe-Mn solid solutions obtained from both EIMs at very low temperature (1 K) Monte Carlo simulations shows the same Mn concentration dependence as predicted by DFT calculations. It tends to be antiferromagnetic to Fe magnetic moments at low concentration (below the transition, which

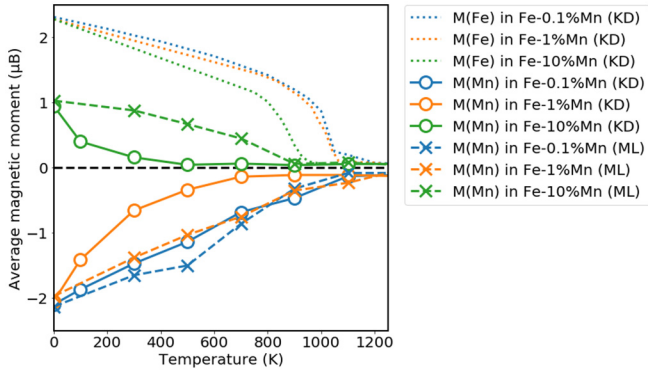

FIG. 13. Temperature evolution of the average magnetic moment of Fe and Mn atoms in bcc Fe-Mn at various concentrations (0.1, 1, and 10% at. Mn). The total magnetization of pure bcc Fe is shown as a black dotted line for shape comparison.

occurs at about 7 at. % Mn) and ferromagnetic at high concentrations.

Using our models with spin Monte Carlo simulations, we determine the evolution of the average magnetic moment of Mn atoms with temperature, at fixed random atomic configurations in order to avoid the appearance of atomic short-range order. Fe-Mn random alloys at 0.1, 1 and 10 at. % Mn are studied, in order to consider both Mn magnetic regimes, below and beyond the Mn magnetic-state transition concentration.

As can be observed in Fig. 13, in both regimes and for both models the absolute value of the average magnetic moment of Mn atoms decreases with temperature faster than the average moment of Fe (which decreases following the evolution of the total magnetization). In the truly isolated-Mn case (0.1 at. % Mn) the decrease is almost linear and the curve reaches 0 approximately at the Curie temperature of the system. For the more concentrated cases, the two parametrizations yield qualitatively different trends. While the ML model predicts an almost linear decrease of the Mn magnetic moment below and above the magnetic-state transition concentration, the decrease is faster in the case of the KD model.

Additional analysis of our data confirms that the magnetic moment magnitude of Mn atoms tends to increase with temperature, from around 1.85 to 2.05 μ_B in the considered temperature range. This attests that the loss of average magnetic moment does not come from the longitudinal spin excitations. A plausible cause of this fast decrease of the average Mn moment magnitude compared to the Fe case is the atypical presence of two magnetic minima for a Mn atom in Fe, namely the AF and the FM states, with a rather small energy difference (0.05 eV for an isolated Mn at 0K). The AF state is the ground state for the isolated Mn, but the FM state becomes gradually populated with increasing temperatures.

For a comparison, we consider the same magnitudes in dilute bcc Fe-Cr alloys, where Cr magnetic moments always tend to be antiparallel to Fe moments [74]. These results however show that the Cr average moment follows the same decrease shape as in the Fe case and at variance with the Mn case.

In order to go further in the analysis, we have determined the ratio of Mn atoms at the FM state (FM-Mn) as a function

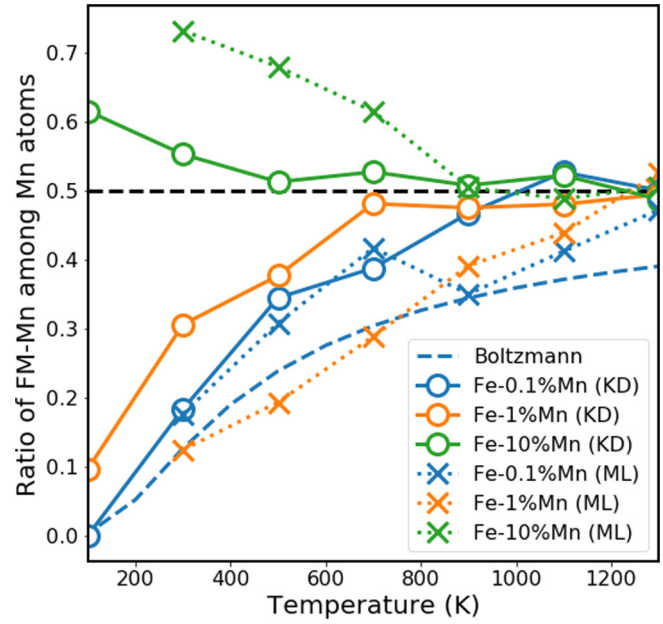

FIG. 14. Temperature dependence of the ratio of FM-Mn among Mn atoms in bcc Fe-Mn at various concentrations (0.1, 1, and 10 at. % Mn). For the case of 0.1 at. % Mn the expected ratio from Boltzmann theory (see text) is shown with the dotted line.

of the temperature. The results are shown in Fig. 14. We can indeed observe that the ratio of FM-Mn atoms at low temperatures is approximately 0% for the 0.1 and 1 at. % Mn concentrations and is above 60% for the 10 at. % Mn case. These results are in agreement with a previous DFT study evidencing that the average magnetic moment of Mn atoms in bcc Fe undergoes a transition from the AF-Mn state at low Mn concentration to the FM-Mn state at high Mn concentration (more than 7 at. % Mn) [25]. As temperature increases, the ratio of FM-Mn evolves towards 50%. The details of the temperature dependence, however, are qualitatively different in both parametrizations, which explains the different behavior in Fig. 13.

We also compared in Fig. 14 the ratio of FM-Mn in the 0.1 at. % Mn system from our Monte Carlo simulations and the expected ratio from the Boltzmann theory, expressed as follows:

$$\frac{N_{\text{FM-Mn}}}{N_{\text{AF-Mn}} + N_{\text{FM-Mn}}} = \frac{\exp\left(\frac{-\Delta E}{k_B T}\right)}{1 + \exp\left(\frac{-\Delta E}{k_B T}\right)} \tag{9}$$

with $N_{\text{FM-Mn}}$ and $N_{\text{AF-Mn}}$ being, respectively, the number of FM-Mn and AF-Mn atoms, and ΔE being the energy difference between FM-Mn and AF-Mn states obtained from DFT calculations ($\Delta E = 0.05$ eV at 0 K predicted by DFT and both models).

We note that as temperature increases, the Fe magnetic state becomes more and more disordered, and the terms AF-Mn and FM-Mn are less and less defined. Especially, at temperatures above the Curie point, as the system is paramagnetic, there is no reason to expect the ratio to follow properly the Boltzmann distribution. We keep classifying Mn atoms depending on the direction of their spins along an arbitrary

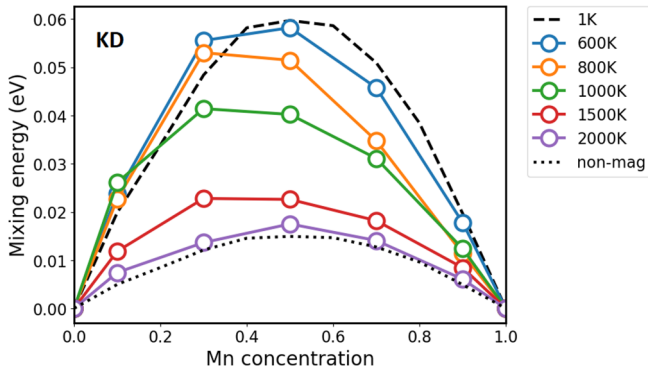

FIG. 15. Mixing energy of random Fe-Mn alloys as a function of Mn atomic concentration for various temperatures. The black dashed line shows the low temperature limit of mixing energy while the black dotted line shows the nonmagnetic contribution, also corresponding to the high temperature limit.

axis in order to illustrate their random distribution at high temperatures.

D. Temperature dependence of Fe-Mn mixing energy

In the previous section, the mixing energy of bcc Fe-Mn random alloys is calculated over the whole range of concentrations at 1 K, using Monte Carlo simulations. Similar spin-MC simulations were performed at various temperatures in order to study the effect of temperature-dependent magnetism on the mixing energy of bcc Fe-Mn alloys.

As shown in Fig. 15, the temperature evolution of the bcc Fe-Mn mixing energy is related to the magnetization. Indeed, for any given concentration, two regimes can be clearly identified: Below the magnetic transition temperature, the mixing energy curve remains quite similar to the 0 K limit, while beyond the magnetic transition temperature, it converges to a high temperature paramagnetic limit. It can also be noticed that at both high and low temperature limits, that is, as soon as for all the concentrations the temperature is located either below or above the magnetic transition temperatures, the mixing-energy curve is symmetric. But, for the intermediate temperatures, an asymmetry appears between the Mn-rich and the Fe-rich domains. Also, the Mn-rich mixing energies decrease faster with increasing temperature than the Fe-rich values. This asymmetry is consistent with the above-mentioned two-regime behavior, considering the difference between the Fe-rich and Mn-rich magnetic transition temperatures. As previously described, we predict the magnetic transition temperature to decrease with Mn concentration (see Fig. 12). Actually, the Mn-rich phase should exhibit a Neel magnetic transition temperature regarding the DFT magnetic ground state, which we cannot reproduce as our model predicts a spin-glass magnetic structure at low temperature in the Mn-rich side.

Please note that the decrease of the mixing energy with temperature is only due to the magnetic contribution as there is no atomic-position changes in these simulations. We notice that the paramagnetic limit (2000 k) of the mixing energy curve is very similar to the nonmagnetic contribution of the 0 K mixing energy (shown in Fig. 15), indicating that the mixing between Fe and Mn atoms has a negligible impact on the average magnitude of their respective magnetic moments. Overall, the present results suggest that spin disordering favors the mixing of Fe and Mn, while spin ordering favors the phase separation tendency.

It is worth mentioning that our results are in qualitative agreement with a previous CALPHAD prediction [23], in which the thermodynamic parameters lead to a fully positive mixing energy of bcc Fe-Mn alloys which decreases with temperature. For the sake of comparison, the mixing energy at 50% at. Mn calculated using the parameters of this study is 0.08 eV at a 1 K temperature (our value being 0.06 eV). Concerning the decrease rate, the KD model predicts that the 50% at. Mn mixing energy converges to 0.015 eV around 2000 K while the mixing energy calculated using the parameters of Ref. [23] shows a slower decrease (0.06 eV at 2000 K). As we have shown in the previous section that the low temperature mixing energy predictions of the ML-model exhibit qualitative differences with DFT results, we chose not to develop the temperature dependence of this property using the ML model.

E. Temperature and concentration evolution of atomic short-range order

The Monte Carlo results presented up to this point are performed by varying only the magnetic configuration of the system while the atomic structure is frozen. In order to go further insights into the interplay between the magnetism and thermodynamic properties versus temperature, it is necessary to follow the evolution of both the magnetic and the atomic structures simultaneously. Therefore, we include, in addition to the Monte Carlo spin equilibration, atomic exchanges on a bcc lattice.

To this end, bcc Fe-Mn alloys were studied at various concentrations and temperatures, in order to evaluate the clustering tendency for both degrees of freedom. We consider the Cowley-Warren formulation of atomic short-range order (ASRO) [75,76], for which the parameter

$$\alpha_i^{\mathrm{Mn}} = 1 - \frac{n_i}{Z_i C_{\mathrm{Fe}}} \tag{10}$$

is averaged over all Mn atoms. Here, n_i is the number of Fe atoms on the ith nearest-neighbor shell of the considered Mn atom, Z_i is the coordination on the i-*nn* shell, and C_{Fe} is the Fe atomic concentration of the system.

The calculated 1*nn*-ASRO is shown in Fig. 16 for a Fe-10 at. %-Mn alloy. The temperature evolution of the reduced magnetization is also given for information. In order to investigate the interplay between the magnetic and chemical orders, similar MC simulations have been performed with a fixed spin temperature T_s, independent of the atomic temperature T. Consistent with Fig. 8, the low temperature ASRO within the KD model is dominated by the magnetic degrees of freedom. Hence, by imposing a 1 K (resp. 2000 K) spin temperature, we find a generally larger (resp. lower) ASRO. A similar trend is also observed with ASRO of farther neighboring shells. We therefore confirm that magnetic ordering enhances the unmixing tendency in bcc Fe-Mn alloys.

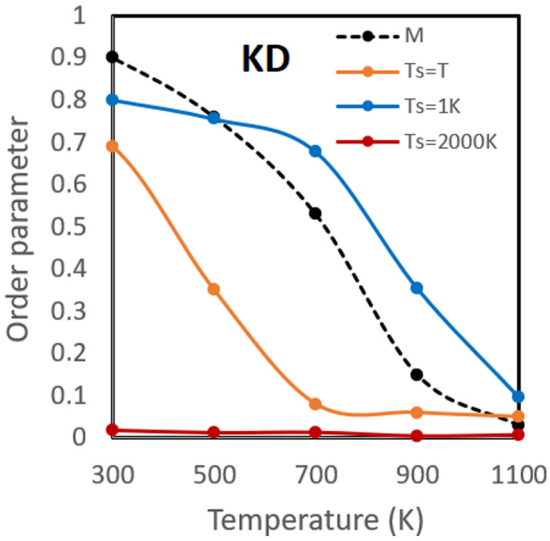

FIG. 16. 1*nn* atomic short range order and reduced magnetization as functions of temperature obtained with the KD model, at a 10 at. % Mn concentration.

TABLE I. KD model: Magnetic and chemical interaction parameters between two atoms, depending on their relative distance, respective species, and the eventual proximity of a vacancy (in meV).

Distance	1*nn*	2*nn*	3*nn*	4*nn*	5*nn*
$J_{\text{Fe-Fe}}$	−3.39	−2.26	−0.83	0.42	0.44
$J_{\text{Mn-Mn}}$	1.51	1.30	0.26	−0.98	0.53
J_0	0.057	0.066	0.042	0.089	0.026
$V_{\text{Fe-Fe}}$	−10.85	8.18	0	0	0
$V_{\text{Mn-Mn}}$	4.63	−1.93	−1.06	−0.19	0.25
$V_{\text{Fe-Mn}}$	−6.09	3.75	0	0	0
$J_0(1nnvac)$	0.232	0.261	0.187	0.327	0.138
$V_{\text{Fe-Mn}}(1nnvac)$	30.2	−17.3	0	0	0
$J_0(2nnvac)$	0.189	0.212	0.151	0.267	0.110
$V_{\text{Fe-Mn}}(2nnvac)$	−30.2	17.3	0	0	0

F. Vacancy properties near a Mn solute

As our KD model also allows to consider the presence of a vacancy, it can be employed to predict the vacancy-Mn interaction properties, particularly the magnetic free energy of binding (accounting for the magnetic entropy) versus temperature. This value dictates the vacancy concentration around Mn, which is especially important for the determination of solute diffusion coefficients via a vacancy mechanism [77,78].

In practice, we calculate the magnetic free energy of formation of a vacancy at a 1*nn* distance of the solute and in a pure Fe lattice, by evaluating an equilibrium vacancy concentration ratio between the system of study at each temperature and a reference system with a known vacancy formation energy (here the perfectly FM bcc Fe) via Monte Carlo simulations, using the same approach as in Ref. [17]. A description is given in Sec. II B. The 1*nn* Mn-vacancy binding free energy results from the difference between these two formation free energies.

The left panel of Fig. 17 shows the vacancy formation magnetic free energy in pure Fe and at 1*nn* sites of a Mn solute in Fe, as functions of temperature. Concerning the pure Fe case, the vacancy formation magnetic free energy obtained in the low and high temperature regimes (respectively, 2.20 and 1.99 eV in FM and PM magnetic states) is in agreement with previous experimental and DFT data from the literature which range from 2.00 to 2.24 eV in the FM state and from 1.54 to 1.98 eV in the PM state [16,79–82]. We note that the vacancy formation magnetic free energy in the PM state shows very scattered results in the literature, which are very sensitive to the computational details, while the various studies are very consistent concerning the FM state [16,79–82]. As can be noticed, at low temperatures the formation free energy at 1*nn* sites of the solute is approximately 0.14 eV lower than the value in pure Fe, which is consistent with the magnetic free

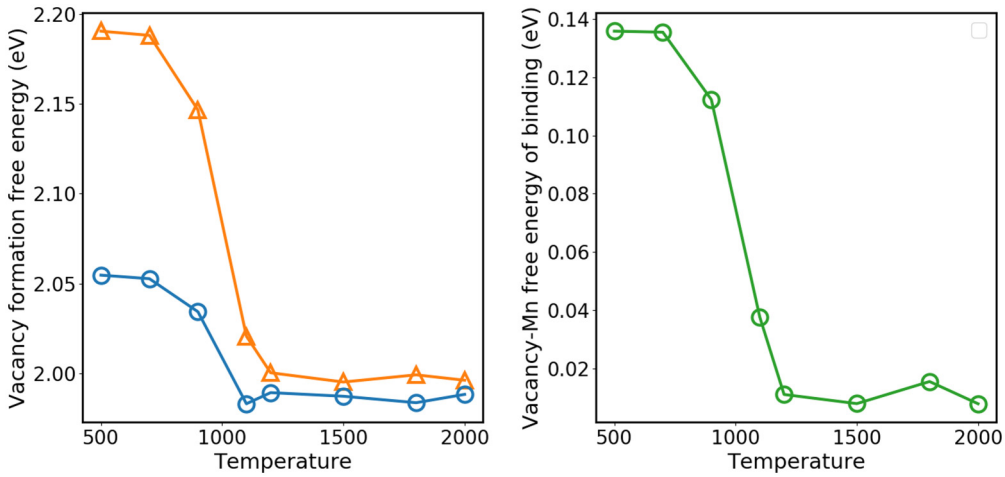

FIG. 17. Left panel: Temperature dependence of the vacancy formation magnetic free energy, in pure Fe (orange) and in the nearest-neighbor shell of a Mn solute (blue). Right panel: Temperature dependence of the vacancy-Mn magnetic free energy of binding. The involved spin-MC simulations adopts a temperature rescaling factor corresponding to a Bose-Einstein statistics, in order to obtain numerical results consistent with the previous study [17]. The same re-scaling factor for pure Fe is applied for the extremely dilute Fe-Mn system.

TABLE II. KD model: Magnetic onsite terms of Fe and Mn atoms, depending on the presence or not of a vacancy (in meV). The superscripts 0, 1, and 2 in this table refer, respectively, to the absence of vacancy in the two nearest neighbor shells of the concerned atom (0), the presence of a vacancy in its first neighbor shell (1), and the presence of a vacancy in its second neighbor shell (2).

Interactions	A^0	B^0	A^1	B^1	A^2	B^2
Fe	−259.0	27.6	−250.2	24.7	−285.7	35.2
Mn	−37.70	6.93	−116.2	8.54	−37.70	6.93

TABLE IV. ML model: Magnetic and chemical interaction parameters between two atoms, depending on their relative distance, and respective species (in meV).

Distance	1*nn*	2*nn*	3*nn*	4*nn*	5*nn*
$J_{\text{Fe-Fe}}$	−14.4	0.03	2.65	0	0
$J_{\text{Fe-Mn}}$	−2.23	0	0	0	4.14
$J_{\text{Mn-Mn}}$	24.29	16.09	−8.96	−10.00	10.00
$V_{\text{Fe-Fe}}$	−1927.36	−0.12	0	0	0
$V_{\text{Mn-Mn}}$	−1188.99	−1302.10	−53.32	−2.86	47.48
$V_{\text{Fe-Mn}}$	−1577.47	−659.95	0	0	0

energy of binding obtained via *ab initio* calculations. This result is also consistent with an earlier study [83] which reports 0.17 eV for the Mn-Vac binding energy in FM Fe. That same study also reports that the vacancy-Mn interaction vanished in the PM state. Also, a previous first-principles work [84] found the Mn-vac binding energy in the FM state to be 0.16 eV. Interestingly, as the temperature increases, this difference decreases towards approximately zero in the fully paramagnetic regime (right panel of Fig. 17). This solute-vacancy binding behavior indicates that the magnetic disorder is able to erase the chemical effects in the very dilute alloys. Since we have observed an identical behavior in the case of Cu solutes in Fe [17], while Cu and Mn have very different magnetic properties, it appears to be a general behavior, independent of the chemical nature of the solute.

VI. CONCLUSIONS

Body-centered cubic Fe-Mn alloys present complex and atypical magnetic-interaction behaviours. Guided by the goal of studying temperature-dependent properties of these alloys, we parameterized an effective interaction model containing explicitly both magnetic and chemical variables. We adopted a knowledge-driven fitting procedure, that is, using only a rather small amount of relevant DFT data. A progressive parametrization strategy was used, which puts emphasis on those data considered to be physically most important. Based on conclusions from DFT studies, one of our assumptions is the dominance of Mn-Mn magnetic interactions over the Fe-Mn ones, in the presence of a magnetic frustration. Also, the atypical presence of two magnetic minima for Mn solutes should be correctly captured. Further, including noncollinear magnetic configurations in the fitting database turned out to be essential for a satisfactory model.

In order to benchmark the model and its dependence on the knowledge-driven assumptions, it was compared with a second parametrization method. To this end, we used a machine-learning technique based on ridge regression for the same training data. Apart from the dependence of the starting values, the resulting model considered all the DFT data simultaneously without bias. Though being aware of the insufficient data density for machine learning techniques, this twofold strategy raised our awareness of strengths and potential imprecision of the knowledge-driven model. It turned out that the magnetic interaction strength is rather independent of the fitting procedure, while the energetic properties such as the mixing enthalpies are much more sensitive to the model parameters. In fact, the energetic properties in the alloys are highly dependent on the magnetism.

Finite temperature Monte Carlo simulations were then performed in order to show the ability of the KD model to predict properties which are not included in the fitting data. For instance, the Mn concentration dependence of the magnetic transition temperature is found in excellent agreement with most experimental results. At variance with most experimental methodologies, only providing averaged properties, our approach allows to access the local magnetic moment around individual atoms. It allowed us to study the temperature evolution of the distribution of the angle between neighboring Fe and Mn spins, along with the evolution of magnitude of Mn magnetic moments. We observed that, contrary to Cr atoms in bcc Fe-Cr alloys, the average magnetic moment of Mn atoms in bcc Fe-Mn does not follow the total magnetization decrease. Indeed, the temperature induced magnetic disordering of Mn atoms is reinforced by the possibility for each spin to switch between the AF-Mn and FM-Mn states.

The temperature dependence of the mixing energy over the whole range of concentration was also determined. The results suggest that the unmixing tendency is highly related to the magnetic order of the system. Moreover, we identified a correlation between the chemical short-range order and the total magnetization of the system. We show that if constraining the spin temperature to asymptotically low or high temperature values highly affects the 1*nn* chemical SRO. This study allowed to further confirm the enhancement of the unmixing tendency by the magnetic ordering.

Finally, we show that it is fully possible to go beyond the ideal defect-free alloys and to consider the presence of a vacancy using such a model. We provided as an example

TABLE III. KD model: Parameters of the polynomial function describing the local Mn concentration dependence of Fe-Mn magnetic interaction parameters (in meV).

Interaction	*a*	*b*	*c*	*d*	*e*
Value (meV)	6.50×10^{-8}	-8.40×10^{-6}	3.83×10^{-4}	-7.16×10^{-3}	3.04×10^{-2}

TABLE V. ML model: Magnetic onsite terms of Fe and Mn atoms (in meV).

Interactions	A	B	C
Fe	−142.70	15.64	0
Mn	−3.83	−2.22	0.34

TABLE VI. ML model: Parameters of the function describing the local Mn concentration dependence of Fe-Mn magnetic interaction parameters (in meV).

Interaction	J_0^n	$\Delta J_{\text{Fe-Mn}}$
Value (meV)	12.87	−5.22

of application the temperature evolution of the vacancy formation magnetic free energy nearby a Mn solute, showing a strong decrease of solute-vacancy binding with the emergence of magnetic disorder. This result is the first key ingredient for the study of Mn solute diffusion in bcc Fe, to which a future paper will be fully dedicated.

ACKNOWLEDGMENTS

The authors would like to thank O. Hedge and Dr. F. Soisson for fruitful discussions. This work was partly supported by the French-German ANR-DFG MAGIKID project (Grant No. HI1300/13-1). *Ab initio* calculations were performed using Grand Equipement National de Calcul Intensif (GENCI) resources under the A0070906020 and A0090906020 projects and the CINECA-MARCONI supercomputer within the SISTEEL project.

APPENDIX: MODEL PARAMETERS

The parameters of the two models are given in Tables I–VI.

[1] A. V. Ruban and V. I. Razumovskiy, Phys. Rev. B **86**, 174111 (2012).
[2] O. Senninger, E. Martínez, F. Soisson, M. Nastar, and Y. Bréchet, Acta Mater. **73**, 97 (2014).
[3] T. Nishizawa and K. Ishida, *Binary Alloys Phase Diagrams 2*, edited by H. Okamoto, P. R. Subramanian, L. Kacprzak (ASM International, Materials Park, Ohio, USA, 1990).
[4] I. Ohnuma, H. Enoki, O. Ikeda, R. Kainuma, H. Ohtani, O. Sundman, and K. Ishida, Acta Materialia **50**, 379 (2002).
[5] T. Sourmail, Progress in Mat. Sci. **50**, 816 (2005).
[6] A. Dick, T. Hickel, and J. Neugebauer, Steel Research Int. **80**, 603 (2009).
[7] M. Lübbehusen, Diploma work, Univ. Münster (1984) (unpublished).
[8] J. Kucera, B. Millien, J. Ruzickova, V. Foldyna, and A. Jakobova, Acta Metall. **22**, 135 (1974).
[9] D. Graham and D. H. Tomlin, Philos. Mag. **8**, 1581 (1963).
[10] J. Geise and C. Herzig, Z. Metallkde. **78**, 291 (1987).
[11] R. J. Borg and B. C. E., Trans. A. I. M. E. **218**, 980 (1960).
[12] C. M. Walter and N. L. Peterson, Phys. Rev. **178**, 922 (1969).
[13] Y. Iijima, K. Kimura, and K. Hirano, Acta Metall. **36**, 2811 (1988).
[14] G. Hettich, H. Mehrer, and K. Maier, Scr. Metall. **11**, 795 (1977).
[15] F. S. Buffington, K. Hirano, and M. Cohen, Acta Metall. **9**, 434 (1961).
[16] S. Huang, D. L. Worthington, M. Asta, V. Ozolins, G. Gosh, and P. K. Liaw, Acta Mater. **58**, 1982 (2010).
[17] A. Schneider, C.-C. Fu, F. Soisson, and C. Barreteau, Phys. Rev. Lett. **124**, 215901 (2020).
[18] J. S. Kirkaldy, P. N. Smith, and R. C. Sharma, Met. Trans. **4**, 624 (1973).
[19] D. Hobbs, J. Hafner, and D. Spisak, Phys. Rev. B **68**, 014407 (2003).
[20] J. Hafner and D. Hobbs, Phys. Rev. B **68**, 014408 (2003).
[21] D. Music, T. Takahashi, L. Vitos, C. Asker, I. A. Abrikosov, and J. M. Schneider, Appl. Phys. Lett. **91**, 191904 (2007).
[22] V. T. Witusiewicz, F. Sommer, and E. J. Mittemeijer, J. Phase Equil. Diff. **25**, 346 (2004).
[23] S. Bigdeli and M. Selleby, Calphad **64**, 185 (2019).
[24] V. I. Anisimov, V. P. Antropov, A. I. Liechtenstein, V. A. Gubanov, and A. V. Postnikov, Phys. Rev. B **37**, 5598 (1988).
[25] A. Schneider, C.-C. Fu, and C. Barreteau, Phys. Rev. B **98**, 094426 (2018).
[26] B. Alling, T. Marten, and I. A. Abrikosov, Nat. Mater. **9**, 283 (2010).
[27] B. Alling, T. Marten, and I. A. Abrikosov, Phys. Rev. B **82**, 184430 (2010).
[28] A. V. Ruban, S. Khmelevskyi, P. Mohn, and B. Johansson, Phys. Rev. B **75**, 054402 (2007).
[29] T. Khmelevska, S. Khmelevskyi, A. Ruban, and P. Mohn, Phys. Rev. B **76**, 054445 (2007).
[30] B. Dutta, S. Bhandary, S. Ghosh, and B. Sanyal, Phys. Rev. B **86**, 024419 (2012).
[31] K. Lagarec, D. Rancourt, S. Bose, B. Sanyal, and R. A. Dunlap, jmmm **236**, 107 (2001).
[32] B. Dutta, F. Köermann, S. Ghosh, B. Sanyal, J. Neugebauer, and T. Hickel, Phys. Rev. B **101**, 094201 (2020).
[33] F. Köermann, A. Dick, B. Grabowski, T. Hickel, and J. Neugebauer, Phys. Rev. B **85**, 125104 (2012).
[34] Y. Ikeda, A. Seko, A. Togo, and I. Tanaka, Phys. Rev. B **90**, 134106 (2014).
[35] V. Pierron-Bohnes, P. Cadeville, and F. Gauthier, J. Phys. F: Met. Phys. **82**, 184430 (1983).
[36] M. Y. Lavrentiev, J. S. Wrobel, D. Nguyen-Manh, and S. L. Dudarev, Phys. Chem. Chem. Phys. **16**, 16049 (2014).
[37] M. Y. Lavrentiev, D. Nguyen-Manh, and S. L. Dudarev, Phys. Rev. B **81**, 184202 (2010).
[38] M. Y. Lavrentiev, J. S. Wrobel, D. Nguyen-Manh, S. L. Dudarev, and M. G. Ganchenkova, J. Appl. Phys. **120**, 043902 (2016).
[39] V. T. Tran, C.-C. Fu, and S. A., Comp. Mater. Sci. **183**, 109906 (2020).

[40] J. B. J. Chapman, P.-W. Ma, and S. L. Dudarev, Phys. Rev. B **99**, 184413 (2019).
[41] P. E. Bloechl, Phys. Rev. B **50**, 17953 (1994).
[42] G. Kresse and D. Joubert, Phys. Rev. B **59**, 1758 (1999).
[43] G. Kresse and J. Hafner, Phys. Rev. B **47**, 558 (1993).
[44] G. Kresse and J. Furthmüeller, Commun. Math. Phys. **6**, 15 (1996).
[45] G. Kresse and J. Furthmueller, Phys. Rev. B **54**, 11169 (1996).
[46] J. P. Perdew, K. Burke, and M. Ernzerhof, Phys. Rev. Lett. **77**, 3865 (1996).
[47] H. J. Monkhorst and J. D. Pack, Phys. Rev. B **13**, 5188 (1976).
[48] M. Methfessel and A. T. Paxton, Phys. Rev. B **40**, 3616 (1989).
[49] C. T. Chen, Y. U. Idzerda, H.-J. Lin, N. V. Smith, G. Meigs, E. Chaban, G. H. Ho, E. Pellegrin, and F. Sette, Phys. Rev. Lett. **75**, 152 (1995).
[50] O. Eriksson, A. M. Boring, R. C. Albers, G. W. Fernando, and B. R. Cooper, Phys. Rev. B **45**, 2868 (1992).
[51] I. Galanakis, Phys. Rev. B **71**, 012413 (2004).
[52] M. Pajda, J. Kudrnovsky, I. Turek, V. Drchal, and P. Bruno, Phys. Rev. B **64**, 174402 (2001).
[53] R. Soulairol, C. Barreteau, and C.-C. Fu, Phys. Rev. B **94**, 024427 (2016).
[54] A. Seko, A. Togo, and I. Tanaka, Phys. Rev. B **99**, 214108 (2019).
[55] A. Takahashi, A. Seko, and I. Tanaka, Phys. Rev. Materials **1**, 063801 (2017).
[56] A. Takahashi, A. Seko, and I. Tanaka, J. Chem. Phys. **148**, 234106 (2018).
[57] X. Li, F. Lou, X. Gong, and H. Xiang, New J. Phys. **22**, 053036 (2020).
[58] C. R. Vogel, *Computational Methods for Inverse Problems*, Vol. 23 (Siam, 2002).
[59] S. Lintzen, J. von Appen, B. Hallstedt, and R. Dronskowski, J. Alloys. Comp. **577**, 370 (2013).
[60] M. Hillert and M. Waldenstrom, Scand. J. Metall. **6**, 211 (1977).
[61] F. Soisson and C.-C. Fu, Phys. Rev. B **76**, 214102 (2007).
[62] L. Messina, N. Castin, C. Domain, and P. Olsson, Phys. Rev. B **95**, 064112 (2017).
[63] F. Keffer, *Handbuch der Physik, 18, pt. 2* (Springer-Verlag, New York, 1966).
[64] E. M. Haines, R. Clauberg, and R. Feder, Phys. Rev. Lett. **54**, 932 (1985).
[65] M. Y. Lavrentiev, S. L. Dudarev, and D. Nguyen-Manh, J. Nucl. Mater. **386**, 22 (2009).
[66] N. B. Melnikov, G. V. Paradezhenko, and B. I. Reser, J. Magn. Magn. Mater. **473**, 296 (2019).
[67] K. Fabian, V. P. Shcherbakov, and S. A. McEnroe, Geochem. Geophys. Geosyst. **14**, 947 (2013).
[68] C. Paduani, E. Galvao da Silva, G. A. Perez-Alcazar, and M. McElfresh, J. Appl. Phys. **70**, 7524 (1991).
[69] S. Arajs, Phys. Stat. Sol. **11**, 121 (1965).
[70] C. Li, F. Sommer, and E. J. Mittemeijer, Mater. Sci. Engin. A **325**, 307 (2002).
[71] C. Sadron, Ann. Phys. Paris **17**, 371 (1932).
[72] H. Yamauchi, H. Watanabe, Y. Suzuki, and H. Saito, J. Phys. Soc. Jpn. **36**, 971 (1974).
[73] V. A. Shabashov, K. A. Kozlov, V. V. Sagaradze, A. L. Nikolaev, K. A. Lyashkov, V. A. Semyonkin, and V. I. Voronin, Philos. Mag. **20**, 560 (2017).
[74] Simulation results from Dr. M. Trochet, CEA Saclay (private communication) (unpublished).
[75] J. M. Cowley, Phys. Rev. **77**, 669 (1950).
[76] B. E. Warren, X-ray diffraction, New York (Dover) (1990).
[77] Y. Adda and J. Philibert, *La Diffusion Dans Les Solides* (Institut national des sciences et techniques nuclaires, 1966).
[78] A. D. Leclaire, *Physical Chemistry: An Advance Treatise* (Academic Press, New York, 1970), Vol. 10.
[79] L. De Schepper, D. Segers, L. Dorikens-Vanpraet, M. Dorikens, G. Knuyt, L. M. Stals, and P. Moser, Phys. Rev. B **27**, 5257 (1983).
[80] H. Wen and C. Woo, J. Nucl. Mater. **470**, 102 (2016).
[81] H. Ding, V. I. Razumovskiy, and M. Asta, Acta Mater. **70**, 130 (2014).
[82] N. Sandberg, Z. Chang, L. Messina, P. Olsson, and P. Korzhavyi, Phys. Rev. B **92**, 184102 (2015).
[83] O. I. Gorbatov, P. A. Korzhavyi, A. V. Ruban, B. Johansson, and Y. N. Gornostyrev, J. Nucl. Mater. **419**, 248 (2011).
[84] O. I. Gorbatov, A. Hosseinzadeh Delandar, Y. N. Gornostyrev, A. V. Ruban, and P. A. Korzhavyi, J. Nucl. Mater. **475**, 140 (2016).